

# Dalton Transactions

Accepted Manuscript



This is an *Accepted Manuscript*, which has been through the Royal Society of Chemistry peer review process and has been accepted for publication.

*Accepted Manuscripts* are published online shortly after acceptance, before technical editing, formatting and proof reading. Using this free service, authors can make their results available to the community, in citable form, before we publish the edited article. We will replace this *Accepted Manuscript* with the edited and formatted *Advance Article* as soon as it is available.

You can find more information about *Accepted Manuscripts* in the [Information for Authors](#).

Please note that technical editing may introduce minor changes to the text and/or graphics, which may alter content. The journal's standard [Terms & Conditions](#) and the [Ethical guidelines](#) still apply. In no event shall the Royal Society of Chemistry be held responsible for any errors or omissions in this *Accepted Manuscript* or any consequences arising from the use of any information it contains.

## ARTICLE

# Structure and Magnetism of a Binuclear Cu<sup>II</sup> Pyrophosphate: Transition to a 3D Magnetic Behaviour Studied by Single Crystal EPR

Cite this: DOI: 10.1039/x0xx00000x

Received 00th November 2014,

Accepted 00th January 2014

DOI: 10.1039/x0xx00000x

www.rsc.org/

Rosana P. Sartoris,<sup>\*a</sup> Otaciro R. Nascimento,<sup>b</sup> Ricardo C. Santana,<sup>c</sup>  
Mireille Percec,<sup>d</sup> Ricardo F. Baggio<sup>e</sup> and Rafael Calvo<sup>\*a,f</sup>

A binuclear Cu<sup>II</sup> compound [Cu<sub>2</sub>(bpa)<sub>2</sub>(P<sub>2</sub>O<sub>7</sub>)(H<sub>2</sub>O)<sub>2</sub>].2.5H<sub>2</sub>O, **1**, (bpa = 2,2'-bipyridylamine), with pairs of Cu<sup>II</sup> ions bridged by one pyrophosphate tetra-anion, was synthesized and crystallized. Its triclinic structure was determined by single-crystal X-ray diffraction. Electron paramagnetic resonance (EPR) spectra of single crystal samples of **1** were recorded for an orientation of the magnetic field (**B**<sub>0</sub>) as a function of temperature (*T*) between 4.7 and 293 K, and at *T* = 4.7, 50 and 293 K, as a function of the orientation of **B**<sub>0</sub>. Below ~8 K the spectra are assigned to two types of mononuclear crystal defects hyperfine coupled to one copper and two nitrogen nuclei. The *g*-matrices and hyperfine couplings at these *T* provide information about the structures of these defects. Above 10 K the spectrum is dominated by the response of the bulk binuclear Cu<sup>II</sup> material, showing hyperfine interactions with two copper nuclei, collapsing to a single peak above 18 K when the units are magnetically connected, and the magnetic behaviour becomes 3D. We attribute the results above 10 K to the interplay of an AFM intrabinuclear exchange interaction  $J_0 = -28(3) \text{ cm}^{-1}$  (defined as  $\mathcal{H}_{\text{ex}} = -J_0 \mathbf{S}_1 \cdot \mathbf{S}_2$ ), and a three orders of magnitude weaker exchange coupling with average magnitude  $|J_1| \sim 0.022 \text{ cm}^{-1}$  between Cu<sup>II</sup> ions in neighbour binuclear units. The interplays between structure, exchange couplings, magnetic dimension and spin dynamics in the binuclear compound are discussed. A previously unreported situation where the structure of the spectra arising from the anisotropic spin-spin interaction term (**D**) within the binuclear unit is averaged out, but the forbidden half field transition is not, is observed and explained.

## Introduction

The diphosphate tetra-anion (P<sub>2</sub>O<sub>7</sub>)<sup>4-</sup> plays important roles in chemical and biochemical processes, such as fat metabolism, and protein, DNA and RNA syntheses.<sup>1,2</sup> In recent years the potential use of metal derivatives of the diphosphate tetra-anion (P<sub>2</sub>O<sub>7</sub>)<sup>4-</sup> as anticancer drugs attracted much attention. Bose *et al.*<sup>3</sup> synthesized and crystallized a class of pyrophosphate complexes of platinum(II) and platinum(IV) exhibiting cytotoxicity comparable to cisplatin and carboplatin. Doyle *et al.*,<sup>1,4-13</sup> investigated the coordination chemistry of metal-pyrophosphate complexes and the concomitant biological, magnetic and catalytic properties of the complexes. Ikotun *et al.*<sup>4</sup> and Marino *et al.*<sup>6</sup> demonstrated that mononuclear and binuclear Co<sup>II</sup>/Ni<sup>II</sup>/Cu<sup>II</sup> pyrophosphates are toxic for drug-resistant lines of cancer cells.

Compounds containing metallic centers connected only by pyrophosphate tetra-anions are rare because of the lability of the tetra anion to hydrolysis, particularly in the presence of divalent metal ions.<sup>1,14,15</sup> Thus, chelating heterocyclic imines as bipyridine, terpyridine or bipyridylamine, have been used to control the self-assembly of Cu<sup>II</sup> species in the presence of (P<sub>2</sub>O<sub>7</sub>)<sup>4-</sup>. Ainscough *et al.*<sup>16</sup> and Xu *et al.*<sup>17</sup> studied the capacity of pyrophosphate ligands to support magnetic interactions between paramagnetic ions. Marino *et al.*<sup>18</sup> investigated the magnetic properties of the copper dimeric compound [Cu(bipy)(cis-H<sub>2</sub>P<sub>2</sub>O<sub>7</sub>)]<sub>2</sub>·3H<sub>2</sub>O (bipy=2,2'-bipyridyne) bridged by the pyrophosphate anion [H<sub>2</sub>P<sub>2</sub>O<sub>7</sub>]<sup>2-</sup>. Within this line of compounds, we reported recently<sup>19</sup> the preparation and structure of two new copper protonated pyrophosphates, and the electron paramagnetic resonance (EPR) spectra of single crystals of these and of two other

related compounds,<sup>18,20</sup> as a function of the orientation of the magnetic field  $\mathbf{B}_0 = \mu_0 \mathbf{H}$  ( $\mu_0$  is the vacuum permeability), and of temperature  $T$  between 4.7 and 293 K. Although the four compounds are binuclear units, their single crystal EPR spectra down to 4 K are characteristic of mononuclear compounds ( $|J_0|/k_B \leq 2$  K), where the intrabinuclear anisotropic spin-spin couplings and the hyperfine couplings with the copper and nitrogen ligands nuclei average out. The structure and magnetic properties of the copper binuclear complex  $10[\text{Cu}_2(\text{bipy})_2(\text{P}_2\text{O}_7)(\text{H}_2\text{O})_2] \cdot n\text{H}_2\text{O}$  containing pyrophosphate tetra-anion bridges have been reported.<sup>5</sup> This paper describes the results of a detailed study of the new binuclear compound  $15[\text{Cu}_2(\text{bpa})_2(\text{P}_2\text{O}_7)(\text{H}_2\text{O})_2] \cdot 2.5\text{H}_2\text{O}$ , **1**, using X-ray crystallography and EPR spectroscopy. The EPR measurements in oriented single crystals show a rich temperature dependent spectrum that allows characterising the magnetic properties, providing a further understanding of the magnetic behaviour of pyrophosphate-bridged binuclear compounds. Besides, the spectra at low  $T$  show traces of crystal defects existing in the  $20$  structure. EPR spectra in powder samples were also recorded, above 77 K but they do not provide additional information. Spectroscopic phenomena at  $T$  below 18 K, arising from the Bose-Einstein condensation<sup>21</sup> of the material and from the dynamics of triplet magnetic excitations,<sup>22,23</sup> are observed and  $25$  explained. The characteristic splitting arising from anisotropic spin-spin interactions ( $D$ -term)<sup>24,25</sup> is averaged out by the interdimeric interactions;<sup>26,27</sup> however, the half field forbidden transition<sup>25,28,29</sup> arising from the same interactions is observed. This apparent contradiction is explained and used to  $30$  estimate the  $D$  term. Our results exemplify further the potentiality of single crystal EPR measurements to understand the electronic structure, magnetic behaviour and spin dynamics of weakly interacting polynuclear compounds with a singlet ground state.<sup>21,27,30,31</sup>

### 35 Experimental Section

Elemental analyses were performed on a Carlo Erba 1108 elemental analyser. IR spectra were recorded in a diamond ATR on a Nicolet 510P FT-IR spectrophotometer. All chemicals, were commercially available of analytical or  $40$  reagent-grade purity and used as received. Water was purified with a Millipore mili-Q system, yielding a resistivity of  $18 \text{ M}\Omega\text{cm}^{-1}$ .

#### Synthesis of 1

The compound was obtained from a solution of copper nitrate  $45$  (1 mmol, 0.241 g) in water (40 mL) to which 2,2'-bipyridylamine (bpa, 1 mmol) was slowly added under stirring at ambient temperature. After that,  $\text{Na}_4\text{P}_2\text{O}_7$  (1 mmol) was added and the pH was adjusted to 2.5 with  $\text{HNO}_3$  to keep the solution clear. The system was filtered and the solution was  $50$  maintained at  $40^\circ\text{C}$ . After two days little pale green rectangular crystals with sizes up to  $\sim 0.5 \times 1 \times 1 \text{ mm}^3$ , of good quality for single crystal X-ray diffraction and EPR measurements, were harvested. The yield in terms of large single crystals for EPR

measurements is low, inhibiting us from preparing isotopically  $55$  enriched single crystals. From the remaining solution maintained at  $40^\circ\text{C}$  crystallized after 20 days the previously reported dehydrated  $[\text{Cu}(\text{bpa})(\text{H}_2\text{P}_2\text{O}_7)]_2$ .<sup>19</sup> Anal. Calcd. for  $\text{Cu}_2\text{C}_{20}\text{H}_{29}\text{N}_6\text{O}_{11.5}\text{P}_2$ : C: 32.85; H: 3.77; N: 11.6; found: C: 32.6; H: 3.7; N: 11.0%. Main IR bands  $60$  (diamond ATR,  $\text{cm}^{-1}$ ): 3400m, vbr, 3079w, 1747w, 1652s, br, 1589m, 1538m, 1481sh, 1475vs, 1429m, 1370w, 1355w, 1236m, 1155, 1110, 1095 (vs), 868(m), 775(s), 578(m), 552(m).

#### Crystal Structure Determination

The crystal structure of **1** was determined at 294 K with an Oxford Xcalibur, Eos, Gemini CCD area-detector diffractometer<sup>32</sup> using graphite-monochromated Mo-K  $\alpha$  radiation ( $\lambda = 0.71069 \text{ \AA}$ ). Data were corrected for absorption with CrysAlisPro,<sup>32</sup> version 1.171.33.6, applying an empirical  $70$  absorption correction using spherical harmonics. The structure was solved by direct methods with SHELXS97,<sup>33</sup> and refined by full-matrix least-squares on  $F^2$  with SHELXL-2014.<sup>33</sup> Hydrogen atoms attached to carbon were added geometrically and refined as riding, both in coordinates as in (isotropic)  $75$  displacement factors. N-H's and O-H's for fully occupied hosts were located in the Fourier difference map, while those for the depleted solvation water molecules were inferred from the H-bonding scheme suggested by the O...O short contacts. In all cases these N-H's and O-H's were refined with restrained  $80$  (O/N)-H: 0.85A(1) and H...H=1.35(1)A distances. Software used to prepare material for publication includes SHELXL-2014<sup>33</sup> and PLATON.<sup>34</sup> Full use of the CCDC package was made for searching in the CSD Database,<sup>35</sup> and for crystal structure visualization.<sup>32,36,37</sup>

#### 85 Electron Paramagnetic Resonance (EPR) Methods

Room  $T$  measurements were performed in single crystal and powder samples using Bruker EMX Plus ( $\sim 9.8 \text{ GHz}$ ) and Varian E110 ( $\sim 34 \text{ GHz}$ ) EPR spectrometers, with cavities  $90$  operating with 100 kHz field modulation. Measurements between 4.7 and 293 K were performed in single crystals with a Bruker Elexsys E580 spectrometer at  $\sim 9.3 \text{ GHz}$ . Magnetic field and signal amplitude calibration at the sample position were achieved using  $\text{Cr}^{\text{III}}:\text{MgO}$  ( $g = 1.9797$ ) and DPPH ( $g = 2.0035$ ) as convenient paramagnetic markers with EPR signals mostly  $95$  outside the field range of the signals of the sample. Microwave power and magnetic field modulation were chosen and kept fixed during all measurements, allowing the spectra to be recorded in the whole range of  $T$  and orientations of  $\mathbf{B}_0$  without saturation or overmodulation of the signals of the sample and  $100$  the markers, within the range of linear response. Spectra obtained from powder samples above 77 K, show little structure, and do not add new information, so are not presented here. The triclinic samples present special difficulties for mounting and orienting single crystals for EPR measurements  $105$  and we describe the used procedures.<sup>19</sup> Crystal habits were identified measuring the angles between edges on each sample

face with a goniometric optical microscope, and comparing the results with crystallographic information.

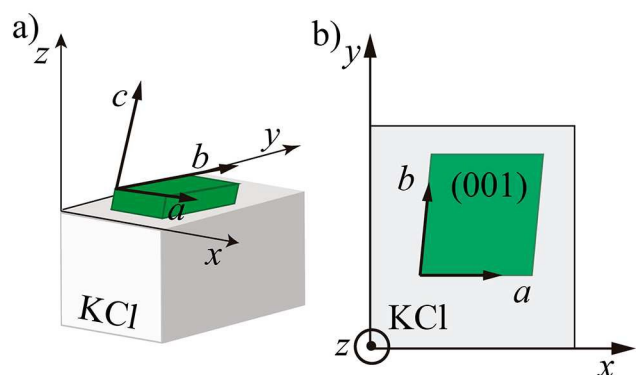


**Fig 1** Sample holder and mounting of the sample for the EPR experiments, displaying the relation between the orthogonal laboratory coordinate system  $xyz$  and the crystal system  $abc$ .

The largest natural growth faces are  $ab$  (001) planes, displaying  $\langle 100 \rangle$  and  $\langle 010 \rangle$  edges. Cubic sample holders made by cleaving pieces of KCl single crystals (Fig. 1) were used to define orthogonal laboratory reference  $xyz$  frames to mount the samples. The  $ab$  crystal faces were glued with vacuum grease to the  $xy$  face of the holder, with a  $\langle 100 \rangle$  edge parallel to the  $x$  edge, so  $x = a$ ,  $z = a \times b / |a \times b| = c^*$  and  $y = z \times x = b^*$ , allowing to obtain the relationship between the laboratory and the triclinic crystal axes.<sup>38</sup> Sample holders were mounted on top of a pedestal inside the cavity with one face ( $xy$ ,  $yz$  or  $xz$ ) parallel to the horizontal plane at 4.7 K, 50 K and 293 K, and the orientation of  $\mathbf{B}_0$  was varied either rotating the holder with a goniometer, or rotating the magnet. EPR spectra were recorded in these orthogonal planes at  $5^\circ$  or  $10^\circ$  intervals along  $180^\circ$ . Positions of axes  $x$ ,  $y$  and  $z$  in these planes were determined within  $\sim 1^\circ$  by comparing results in the three planes. Single crystal EPR spectra were also obtained as a function of  $T$  between 4.7 K and 293 K with  $\mathbf{B}_0$  at  $\phi = 132^\circ$  with the  $x$ -axis, in the  $xy$  plane where, according angular dependent measurements at 4.7 K, the spectrum displays maximum resolution. The procedures followed indicated that the sample does not change irreversibly within thermal cycles between 4 and 293 K, showing for different cycles at equal  $T$  the same spectra. We performed spectral simulations using Easyspin,<sup>39</sup> a package of programs working under Matlab,<sup>40</sup> and home-made Matlab programs of our lab.

### Crystallographic Results

Crystallographic data of **1** are given in Table 1 and selected bond distances and angles in Table 2. Figure 2 presents an ellipsoid plot of the asymmetric unit showing the labelling scheme. The molecule displays a central  $\mu_2\kappa^4$ - $\text{P}_2\text{O}_7^{4-}$  unit bridging two independent  $\text{Cu}^{\text{II}}$  centres (Cu1 and Cu2 at 4.983 Å), with two outermost bpa ligands (A and B), and two coordinated water molecules (O1W, O2W) completing the coordination of the metal centres. The structure is further stabilized by two and a half water molecules per formula unit,

**Table 1** Crystallographic details for compound **1**.

Crystal data	
Chemical formula	$\text{P}_2\text{O}_7(\text{C}_{10}\text{H}_9\text{N}_3)_2\text{Cu}_2(\text{H}_2\text{O})_2 \cdot 2.5(\text{H}_2\text{O})$
$M_r$	724.50
Crystal system, space group	Triclinic, $P\bar{1}$
Temperature (K)	294
$a, b, c$ (Å)	7.6495 (17), 9.511 (2), 18.497 (4)
$\alpha, \beta, \gamma$ ( $^\circ$ )	82.343 (4), 87.017 (4), 84.233 (4)
$V$ (Å <sup>3</sup> )	1326.0 (5)
$Z$	2
Radiation type	Mo $K\alpha$
$\mu$ (mm <sup>-1</sup> )	1.80
Crystal size (mm)	0.28 × 0.18 × 0.10
Data collection	
Diffractometer	Oxford Diffraction Gemini CCD S Ultra diffractometer
Absorption correction	Oxford Diffraction, Multi-scan <i>CrysAlis PRO</i>
$T_{\text{min}}, T_{\text{max}}$	0.70, 0.88
No. of measured, independent and observed [ $I > 2\sigma(I)$ ] reflections	11108, 5657, 4401
$R_{\text{int}}$	0.028
$(\sin \theta/\lambda)_{\text{max}}$ (Å <sup>-1</sup> )	0.658
$R[F^2 > 2\sigma(F^2)], wR(F^2), S$	0.042, 0.102, 0.997
No. of reflections	5657
No. of parameters	430
No. of restraints	11
H-atom treatment	H atoms treated by a mixture of independent and constrained refinement
$\Delta\rho_{\text{max}}, \Delta\rho_{\text{min}}$ (e Å <sup>-3</sup> )	0.64, -0.46

**Table 2** Selected geometric parameters (Å,  $^\circ$ ) for compound **1**.

Cu1 coordination polyhedron		Cu2 coordination polyhedron	
Cu1-O2	1.941 (2)	Cu2-O1	2.013 (2)
Cu1-O6	1.989 (2)	Cu2-N2B	2.014 (3)
Cu1-N1A	1.990 (3)	Cu2-O2W	2.342 (3)
Cu1-N2A	1.998 (3)	Cu2-O7	1.929 (2)
Cu1-O1W	2.266 (3)	Cu2-N1B	1.974 (3)
O2-Cu1-O6	92.04 (10)	O7-Cu2-N1B	167.81 (12)
O2-Cu1-N1A	167.04 (11)	O7-Cu2-O1	95.55 (10)
O6-Cu1-N1A	90.04 (11)	O7-Cu2-O2W	82.70 (10)
O2-Cu1-N2A	87.22 (11)	O7-Cu2-N2B	91.22 (11)
O6-Cu1-N2A	171.67 (11)	N1B-Cu2-O2W	87.67 (11)
N1A-Cu1-N2A	88.87 (12)	N1B-Cu2-O1	91.43 (11)
O2-Cu1-O1W	97.29 (10)	N1B-Cu2-N2B	91.41 (12)
O6-Cu1-O1W	99.79 (10)	O1-Cu2-N2B	132.55 (11)
N1A-Cu1-O1W	94.95 (11)	O1-Cu2-O2W	87.27 (10)
N2A-Cu1-O1W	88.53 (11)	N2B-Cu2-O2W	140.18 (11)

one of them of full occupancy (O3W) and the remaining 1.5 accounted for three disordered moieties of half occupancy

(O4W, O5W, O6W). Both copper atoms are penta-coordinated, but their environments have clearly different geometries. The

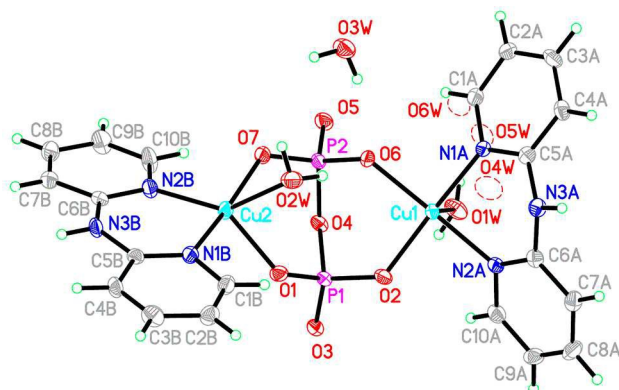


**Fig 2:** Molecular diagram of  $\text{Cu}_2(\text{bpa})_2(\text{P}_2\text{O}_7)(\text{H}_2\text{O})_2 \cdot 2.5\text{H}_2\text{O}$ , **1**; displacement ellipsoids are drawn at a 40% probability level. bpa molecules A and B are associated to Cu1 and Cu2, respectively.

one around Cu1 is a rather regular square pyramid (SP), with N1A, N2A, O2 and O6 defining the base, and the apical position being occupied by the coordinated water molecule O1W. In this environment the copper cation is shifted 0.1803(4) Å from the basal least squares plane, towards the apex, with the Cu1–O1W vector deviating 5.7(2)° from the normal to the plane. This Cu1 coordination polyhedron is fairly regular and imposes some restraints to the N–Cu–N angle resulting in a large distortion from planarity of the attached bpaA ligand, with the py units defining a py–py dihedral angle  $\Delta_{\text{bpaA}} = 37.5(2)^\circ$ . Contrasting with this geometry, the environment of Cu2 is described as a distorted trigonal bipyramid (TB), with O1, N2B and O2W in the basal plane, leaving Cu2 0.009 Å out of the plane, and O7 and N1B at the

**Table 3** Hydrogen-bridges geometry (Å, °) for compound **1**.

N	D—H···A	D—H	H···A	D···A	D—H···A
#1	O2W—H2WA···O6	0.85 (1)	2.26 (2)	3.050 (3)	154 (4)
#2	O2W—H2WB···O3 <sup>i</sup>	0.85 (1)	1.82 (1)	2.672 (3)	177 (4)
#3	N3B—H3NB···O3 <sup>ii</sup>	0.85 (1)	2.01 (1)	2.851 (4)	171 (4)
#4	N3A—H3NA···O5 <sup>iii</sup>	0.85 (1)	1.97 (1)	2.818 (4)	172 (4)
#5	C3B—H3B···Cg3 <sup>iv</sup>	0.93	2.70	3.496 (4)	144
#6	O1W—H1WA···O3W <sup>v</sup>	0.85 (1)	1.96 (1)	2.802 (4)	172 (3)
#7	O1W—H1WB···O5W	0.85 (1)	1.97 (2)	2.771 (6)	159 (4)
#8	O1W—H1WB···O6W <sup>vi</sup>	0.85 (1)	2.03 (1)	2.866 (6)	170 (4)
#9	O3W—H3WA···O6	0.85 (1)	2.05 (1)	2.884 (3)	168 (3)
#10	O3W—H3WB···O3 <sup>i</sup>	0.85 (1)	2.10 (2)	2.912 (3)	162 (4)
#11	C4A—H4A···O5W <sup>vii</sup>	0.93	2.49	3.412 (7)	172
#12	O4W—H4WA···O3W <sup>v</sup>	0.85 (1)	2.06 (2)	2.905 (6)	173 (8)
#13	O5W—H5WA···O5 <sup>vi</sup>	0.85 (1)	1.90 (3)	2.680 (6)	153 (7)
#14	O6W—H6WA···O5	0.85 (1)	1.84 (2)	2.675 (6)	169 (8)

Symmetry codes: (i) x, y+1, z; (ii) -x+1, -y, 1-z; (iii) x-1, y, z; (iv) x+1, y, z, (v) -x+1, -y+1, -z+2; (vi) -x+1, -y+1, -z; Centroid codes Cg3: N2A, C6A, C7A, C8A, C9A, C10A.

The first entry in Table 3 (#1) corresponds to the sole relevant intramolecular H-bond in the structure, and involves one of the O2W hydrogens. The remaining one, as well as the amino H3Nb (#2, #3 in Table 3) are involved in the formation of broad 1D structures (Fig. 3a), embedding different inversion

apices, with the Cu2–O7 and Cu2–N1B vectors subtending angles of 9.4(2) and 2.9(2)°, respectively, to the normal to the plane. This particular TB geometry gives room to a more open N–Cu–N angle allowing for an almost planar bpaB geometry, with py–py dihedral angle  $\Delta_{\text{bpaB}} = 6.8(2)^\circ$ . The pyrophosphate anion is metrically normal, with the P–O bonds of the two non coordinated oxygens slightly shorter than the coordinated ones. The symmetry of the group tends to  $C_m$ , with a deviation of the individual phosphates slightly rotated by  $\sim 12^\circ$  in opposite directions relative to the central P–O–P plane. Bond valence calculations resulted in 2.166 bvu for Cu1 and 2.12 bvu for Cu2.<sup>41</sup> The structure of **1** is topologically quite similar to  $[\text{Cu}_2(\text{bipy})_2(\text{P}_2\text{O}_7)(\text{H}_2\text{O})_2] \cdot 7\text{H}_2\text{O}$ , **2**, previously reported by Kruger *et al.*,<sup>5</sup> with a central  $(\text{P}_2\text{O}_7^{4-})$  bridge connecting the two pentacoordinated  $\text{Cu}^{\text{II}}$  cations in a  $\mu_2\kappa^4$  fashion, the lateral bpa/bipy chelating the cations, and a lone aqua completing the  $\text{CuO}_3\text{N}_2$  cores. Comparing the stereo disposition of both, two salient differences are noted, *i*) the relative positioning of the coordinated water molecules, which in **1** are *trans*, and accordingly non-interacting, whereas *cis* and interconnected through H-bonding in **2**; *ii*) a large distortion from planarity of bpaB in **1** and planarity of the bpaA ligand in **1**, and *iii*) nearly planar bipy units, with inter-bipy dihedral angles  $\Delta_{\text{bipyA}} = 3.8(3)$ ,  $\Delta_{\text{bipyB}} = 3.6(3)^\circ$  associated with a smaller distortion from a “mirror” symmetry in the central pyrophosphate bridge of  $5^\circ$  in **2**. These differences in the distortions of the  $\text{CuO}_3\text{N}_2$  environments from regular SP or TP geometries are reflected by their  $\tau$  parameters<sup>42</sup> ( $\tau = 0.0$  for a square pyramid (SP); 1.0 for a trigonal bipyramid (TB)). Corresponding values of  $\tau$  for Cu1, Cu2 are 0.08, 0.46 and 0.02, 0.19 for **1** and **2** respectively. Compound **1** presents many active sites for hydrogen and  $\pi$ - $\pi$  interactions described in Tables 3 and 4, respectively.

centres and defining tetranuclear dimeric structures linked along  $\langle 100 \rangle$ . This linkage is enhanced by the concatenation of  $\pi$ - $\pi$  interactions involving bpaB (Table 4, #15 and #16).

**Table 4**  $\pi\cdots\pi$ -interactions geometry ( $\text{\AA}$ ,  $^\circ$ ) for compound **1**.

#N	Cg...Cg	icd ( $\text{\AA}$ )	da $^\circ$	mipd ( $\text{\AA}$ )
15	Cg2...Cg4 <sup>ii</sup>	3.892(2)	6.8(2)	3.74(3)
16	Cg2...Cg4 <sup>vii</sup>	3.782(2)	6.8(2)	3.54(1)
17	Cg1...Cg1 <sup>v</sup>	3.561(2)	0	3.420(2)

icd: intercentroid distance; da: dihedral angle; mipd: mean interplanar distance, or mean distance from one centroid to the opposite plane.

Symmetry codes: (viii)  $-x+1, -y, -z$ ; (ix)  $-x+1, -y+1, -z+1$ ; (x)  $-x+2, -y, 1-z$ ; Centroid codes: Cg1: N1A, C1A, C2A, C3A, C4A, C5A; Cg2: N1B, C1B, C2B, C3B, C4B, C5B; Cg4: N2B, C6B, C7B, C8B, C9B, C10B.

Figure 3b displays the same structure as Fig. 3a, now projected along  $a$ , and showing the individual  $\langle 100 \rangle$  “strips” downwards (one of them is highlighted in a coloured background). It shows the way in which these structures are linked by the remaining amino bonds and a C–H... $\pi$  bond (#4 and #5 in Table 3) forming broad planar arrays parallel to (001). All the remaining H-bonding interactions (#6 to #14 in Table 3) are mediated by the hydration water molecules, be it as donors or as acceptors, and serving to link planes along  $\langle 100 \rangle$ . Table 4 (#17) and Fig. 3b show the same effect for the remaining  $\pi\cdots\pi$  interaction. The final result is a strongly connected 3D structure.

### EPR Results

We hereby present the observed spectra with a basic interpretation; followed further by pertinent sections with a detailed analysis.

### Variation of the Spectra with the Temperature $T$

Figure 4 displays selected EPR spectra ( $d\chi''/dB_0$ ) recorded in the  $T$  range between 4.7 and 50 K for  $B_0$  at  $\phi = 132^\circ$  with the  $x$  axis in the  $xy$  plane (Fig. 1 and inset of Fig. 4). According to preliminary measurements in this field orientation the spectra display the greatest resolution in the whole  $T$  range. All spectra recorded at  $T \leq 50$  K are shown in Fig. S1.<sup>†</sup> The spectral changes above 50 K are small and the results are not included.

At  $T = 4.7$  K (Fig. 4a) the spectrum corresponds to  $S = \frac{1}{2}$  spins, with four groups of peaks assigned to the hyperfine splitting with the nuclear spins of copper. Each group shows further splitting due to super hyperfine coupling with two  $^{14}\text{N}$  ligands ( $I_{\text{N}} = 1$ ). The existence of two natural isotopes of copper (63%  $^{63}\text{Cu}$  and 65%  $^{65}\text{Cu}$ ) with spins  $^{63}\text{I}_{\text{Cu}} = ^{65}\text{I}_{\text{Cu}} = 3/2$ , and magnetic moments differing by  $\sim 7\%$ , reduces the resolution of the hyperfine structure. Powder samples for EPR enriched with only one copper isotope<sup>43,44</sup> may be feasible to improve the resolution but isotopically enriched single crystals become too expensive for compound **1**, as described in the experimental section. Figure 5 displays a spectrum obtained at 4.7 K for an orientation of  $B_0$  at  $55^\circ$  off the  $z$ -axis in the  $yz$  plane (see inset). The higher resolution allows observing contributions from two types of defects ( $M_1$  and  $M_2$ ) containing mononuclear Cu ions, both displaying super hyperfine splittings with two nitrogen

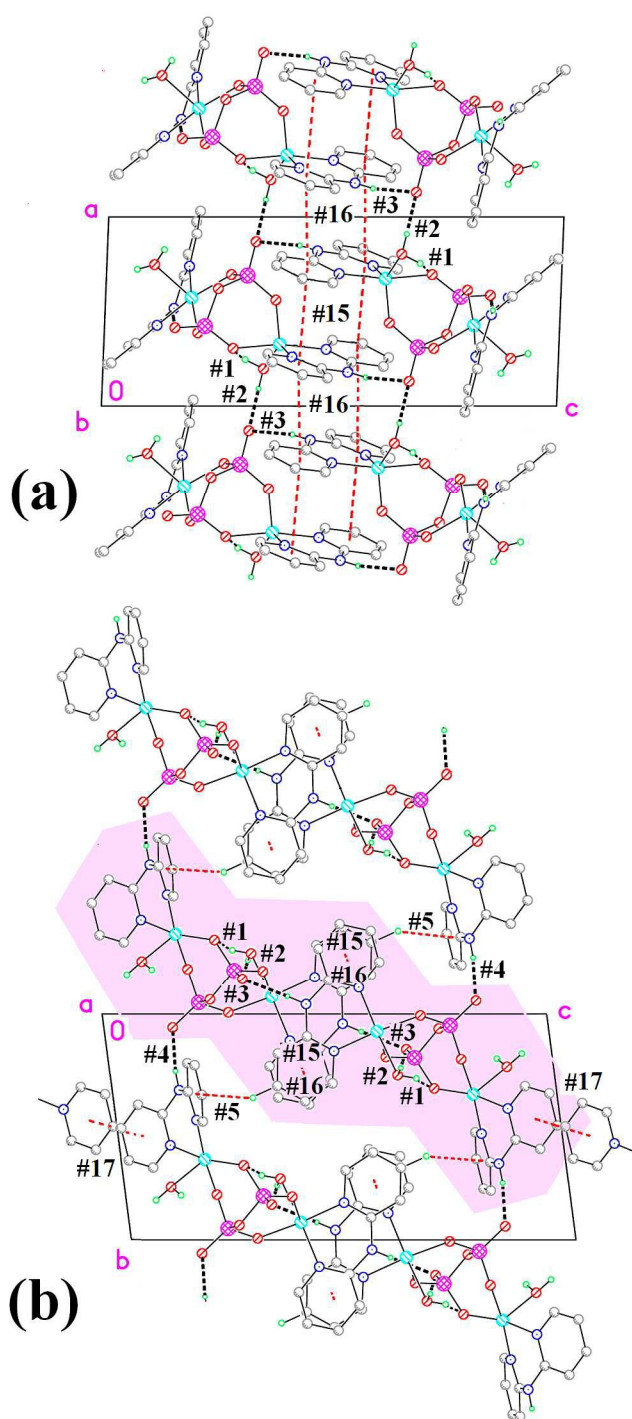


**Fig 3** Packing views of  $\text{Cu}_2(\text{bpa})_2(\text{P}_2\text{O}_7)(\text{H}_2\text{O})_2 \cdot 2.5\text{H}_2\text{O}$ , **1**: (a) Projected down  $a$ , showing the formation of  $\langle 100 \rangle$  strips. (b) Projected down  $b$ , showing the way in which strips interact to form broad planes parallel to (001). N–H...O and O–H...O interactions represented by black broken lines; C–H... $\pi$  and  $\pi\cdots\pi$  ones by red broken lines. All interactions are identified by their # codes in Tables 3 and 4.

ligands. The lower intensity of one group indicates smaller population of species  $M_2$ , that is also present in the spectra of Figure 4a, but with a much weaker contribution as  $M_1$ . A Curie

$1/T$  dependence of intensity of spectra  $M_1$  and  $M_2$  and a loss of resolution of the N hyperfine structure with increasing  $T$  are

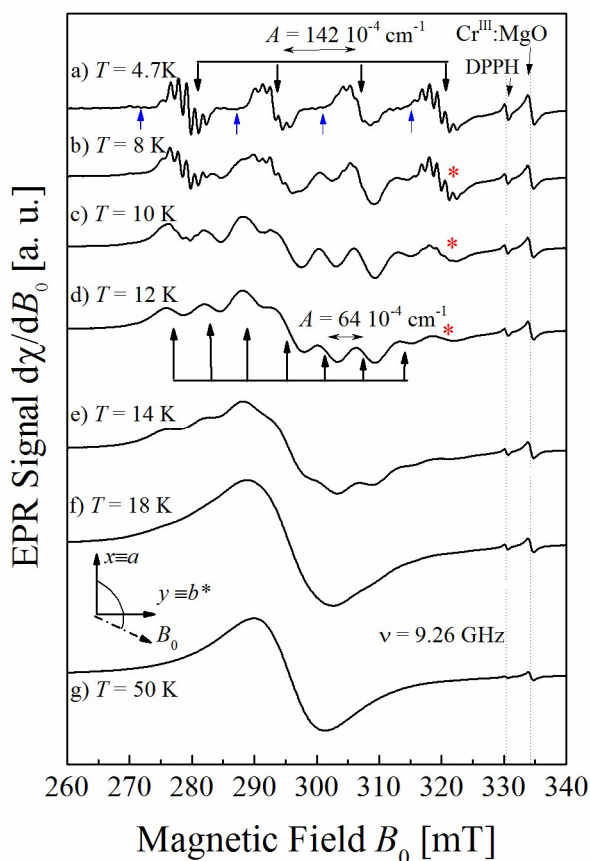


**Fig 4** EPR spectra of a single crystal of 1 observed at 9.26 GHz for  $B_0$  along  $\phi = 5132^\circ$ ,  $\theta = 90^\circ$  in the frame  $xyz$  (see Fig 1 and inset) as a function of  $T$  between 4.7 K and 50 K, a-g. Spectra a) and d) correspond to two different spin systems and the sets of four and seven black arrows indicate the centers of the resonances of the mononuclear defect  $M_1$  and of the binuclear unit, respectively. The ongoing blue arrows in a) indicate the positions of the weak second group of resonances (site  $M_2$ , see text). The red (\*) stars in b, c, d indicate the position of the fourth group of resonances of  $M_1$ , also appearing in the (mainly) binuclear response of spectra in Figs. 4d and  $S3^\dagger$ .

observed. At 8 and 10 K (Figs. 4b,c), the defect contribution to the spectra show increasing broadening and weakening of the hyperfine peaks, and competes with the simultaneous growth in intensity of another spectrum clearly observed at 12 K (Fig. 4d and  $S3^\dagger$ ), presenting seven hyperfine peaks (marked with a set of seven black arrows) with amplitudes approximately proportional to the sequence  $\sim 1:2:3:4:3:2:1$ . They have  $\sim$ half the copper hyperfine splitting in Figs. 4a,b and are assigned to binuclear units with two  $S = 1/2$  spins, each one coupled to its nuclear spin  $I_{Cu} = 3/2$ .<sup>24,25,45</sup> At 12 K (Figs. 4d and  $S3^\dagger$ ) no binuclear fine structure ( $D$ -term) and no hyperfine structure with the N ligands is resolved. Above 14 K (Figs. 4e,f,g) hyperfine structures are broadened and collapsed, ending up in a single broad peak that increases intensity with increasing temperature, reaching a maximum at  $T$  around  $\sim 30$  K, and then decreasing, as expected for an AFM binuclear unit.<sup>27,31,46</sup>

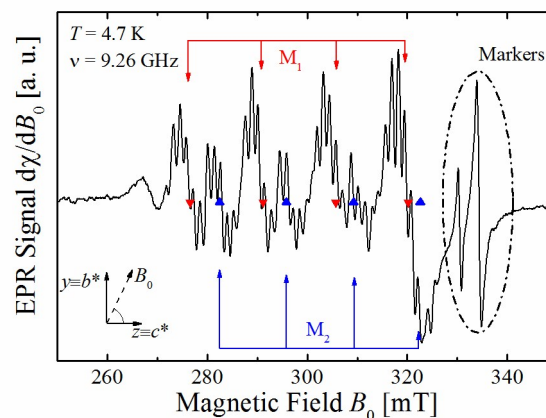


**Fig 5** EPR spectrum observed at 9.26 GHz and 4.7 K for the magnetic field direction  $\theta = 55^\circ$  and  $\phi = 90^\circ$  in the laboratory coordinate frame  $xyz$  (see Fig 1 and inset). For this field orientation the two sets of four groups of lines having different intensities are attributed to mononuclear defect  $M_1$  and  $M_2$ . Down (red) and up (blue) arrows and triangles indicate the centers of the copper hyperfine groups of these sites. The peak at  $B_0 \sim 269$  mT was not identified.

### Variation of the Spectra with Field Orientation at 4.7, 50 and 293 K

Spectra recorded at  $5^\circ$  intervals of  $B_0$  along  $180^\circ$ , in the laboratory planes  $xy$ ,  $xz$  and  $zy$ , at 4.7 K and 9.26 GHz are similar to those in Figs. 4a and 5, showing hyperfine coupling with the copper nuclei and, at some orientations, with two N ligands. The centers of the more intense set of lines  $M_1$  are calculated in the three planes and shown in Figs. 6a,b,c, in which the barycenters of the sets for each field orientation (dashed lines) are used to obtain the  $g$ -values, while the average splitting  $\langle \Delta H_{hyp} \rangle$  between peaks of the groups are related to the copper hyperfine coupling,  $A = g\mu_B \langle \Delta H_{hyp} \rangle$  of  $M_1$ .<sup>25,47,48</sup> The values of  $g^2$  and of  $g^2 A^2$  calculated for  $M_1$  from the results in Figs. 6a,b,c are displayed in Figs. 7a,b. For some orientations of  $B_0$ , mainly in the planes  $zy$  and  $zx$ , we also obtained (Figs.  $S4a,b,c^\dagger$ ) the variation with orientation of  $B_0$  of the group  $M_2$  shown in Fig. 5. The corresponding angular variations of  $g^2$  and  $g^2 A^2$  of  $M_2$  (Fig.  $S5a,b^\dagger$ ) are less accurate than those in Figs. 6 and 7 for  $M_1$ . The position of the single resonance with no binuclear or hyperfine structure observed at  $T = 50$  K and 293 K (Fig. 4g) was calculated for all field orientations,

$$B_0 = B_0 \mathbf{h} = B_0 (\sin\theta \cos\phi, \sin\theta \sin\phi, \cos\theta) \quad (1)$$

by least-squares fits of the observed spectra to Lorentzian derivative line shapes. Figs. 8a,b,c display the corresponding squared  $g$ -factor  $g^2(\theta, \phi)$  at 33.9 GHz and  $T = 293$  K, a), at 9.8 GHz and  $T = 293$  K, b), and at 9.26 and  $T = 50$  K, c), in the three planes of the system  $xyz$ .

### Half Field Contribution to the Spectrum

An important component of the EPR spectra of binuclear units is the (forbidden) transition between the components  $M = \pm 1$  of the triplet state.<sup>25</sup> This transition has been used as one fingerprint of the binuclear behavior for units with spins  $1/2$  and allows to calculate the value of  $D$  and the distance between

spins from powder and single crystal data.<sup>28,29</sup> Evaluating the interspin distance is not a relevant issue when the structure is

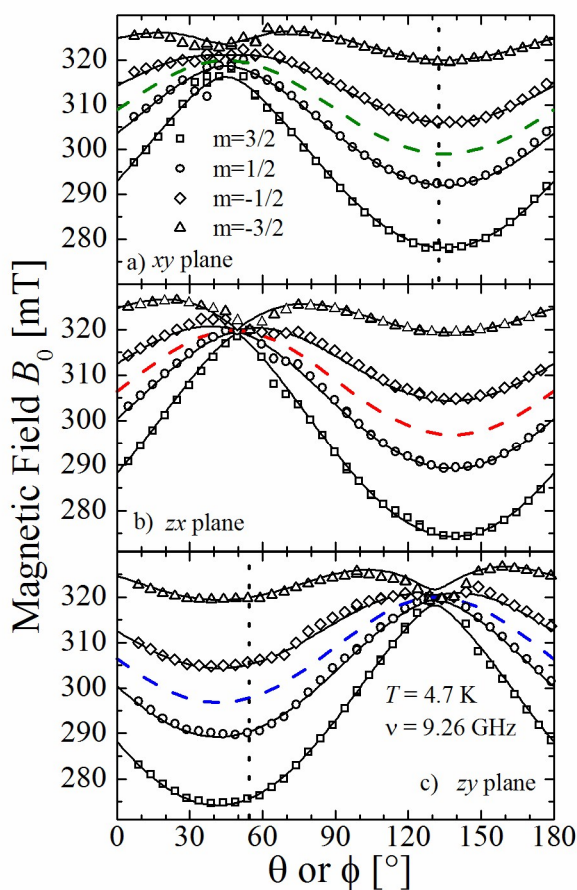


**Fig 6** Angular variation of the field positions of the barycenters of the group of resonances  $M_1$  at  $T = 4.7$  K and 9.26 GHz, for  $B_0$  applied in the  $xy$ ,  $zx$  and  $zy$  laboratory planes. Colored dashed lines in a), b) and c) display the average field of the four hyperfine components. The dotted vertical line in a) indicates the field orientation where the data in Figures 4 were obtained. The dotted line in c) is the orientation where the spectrum in Fig 5 was obtained.

determined, but other previously unknown results arised from a study of the half field resonance in 1. Fig. 9 displays the EPR spectrum of 1 observed between 100 and 400 mT at 12 K at  $70^\circ$  with the x-axis in the  $xy$  plane. This orientation (indicated with an arrow in Fig. 8c). This orientation was chosen because the  $g$ - and hyperfine factors are smallest, and consequently is the hyperfine splitting. The inset displays with a vertical amplification  $\times 1000$  the signal observed around 160 mT. Fig. 9 indicates that the ratio of the areas of the large peak observed around  $g = 2$ , to the small half field peak is  $\sim 1000$ . For higher accuracy, the signal was double integrated to determine the area and the result is identical within an uncertainty of  $\sim 20\%$  arising from the baseline (Fig. S6).<sup>†</sup> The T dependence of of the intensity of the half field peak was studied up to 30 K and is similar to that of the main peak, but the uncertainty is much larger (Fig. S7).<sup>†</sup>

### Analysis of the EPR Data

We analyse here the spectra of the two kinds of spin systems contributing in different  $T$  ranges. In addition, when increasing  $T$ , the defects interact with the binuclear units and the binuclear units between themselves, each interaction producing characteristic effects in the spectra.

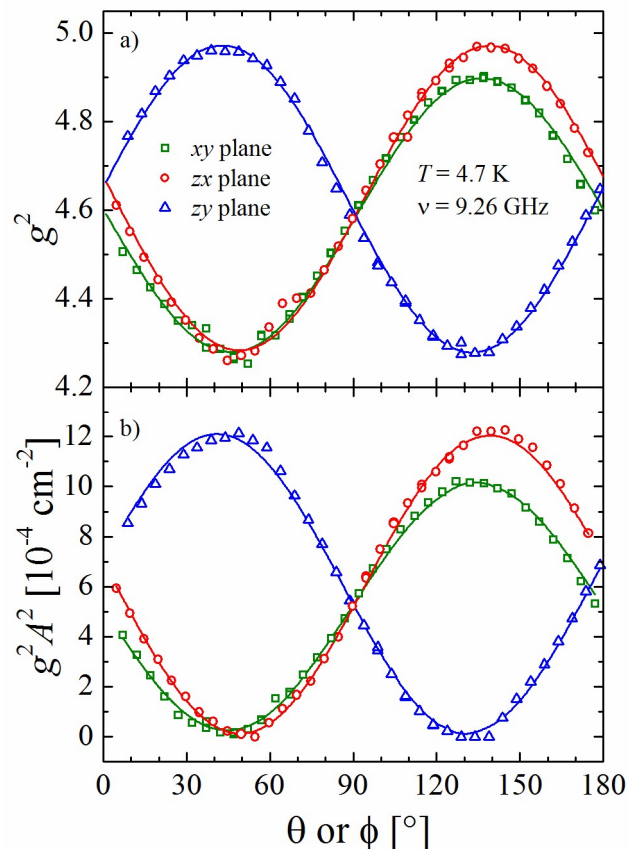


**Fig 7** Values of  $g^2$  and  $g^2A^2$  at 4.7 K calculated for site  $M_1$  from the data in Figure 6. The solid lines are calculated with the components of the  $g^2$  and  $g^2A^2$  matrices given in Table 5.

### The Bulk Binuclear Material

The energy levels of a binuclear unit  $u$  (Fig. 2) are described by the spin Hamiltonian:<sup>25</sup>

$$\mathcal{H}_u = -J_0 \mathbf{S}_{Cu1} \cdot \mathbf{S}_{Cu2} + \mathbf{S}_{Cu1} \cdot \mathbf{D} \cdot \mathbf{S}_{Cu2} + \sum_j \{ \mu_B \mathbf{B}_0 \cdot \mathbf{g}_{Cu_j} \cdot \mathbf{S}_{Cu_j} + \mathbf{I}_{Cu_j} \cdot \mathbf{A}_{Cu_j} \cdot \mathbf{S}_{Cu_j} \} + \sum_j \{ \mathbf{I}_{N1j} \cdot \mathbf{A}_{N1j} \cdot \mathbf{S}_{Cu_j} + \mathbf{I}_{N2j} \cdot \mathbf{A}_{N2j} \cdot \mathbf{S}_{Cu_j} \} \quad (2)$$

where  $\mu_B$  is the Bohr magneton,  $\mathbf{S}_{Cu_j}$  ( $j = 1, 2$ ) are the effective spins of the two copper ions ( $S = 1/2$ ) and their  $g$ -matrices define the Zeeman contribution. The isotropic binuclear exchange coupling  $\mathcal{H}_{ex} = -J_0 \mathbf{S}_{Cu1} \cdot \mathbf{S}_{Cu2}$  (AFM for  $J_0 < 0$ ) displaces the triplet state above the ground singlet state by an amount  $\Delta E = |J_0|$ . The traceless spin-spin interaction matrix  $\mathbf{D}$  considers anisotropic spin-spin couplings (dipole-dipole or anisotropic exchange), splitting the triplet state.  $\mathbf{I}_{Cu_j}$ ,  $\mathbf{I}_{N1j}$  and  $\mathbf{I}_{N2j}$  are the nuclear spins of Cu and their N ligands, and  $\mathbf{A}_{Cu_j}$ ,  $\mathbf{A}_{N1j}$  and  $\mathbf{A}_{N2j}$  the corresponding hyperfine matrices.<sup>25,45</sup> The EPR behaviour expected from eqn 2 is similar to that for an effective spin  $S = 1$ , with two allowed transitions,  $S_z = \pm 1 \leftrightarrow$

0.<sup>25</sup> The matrices  $\mathbf{g}$  and  $\mathbf{D}$  could be evaluated from the angular variation of the positions of these peaks. The hyperfine couplings with each nuclear spin  $I$  split these transitions in  $2I+1$

show the binuclear characteristics (i) and (ii), and (iv) but fail to show (iii).

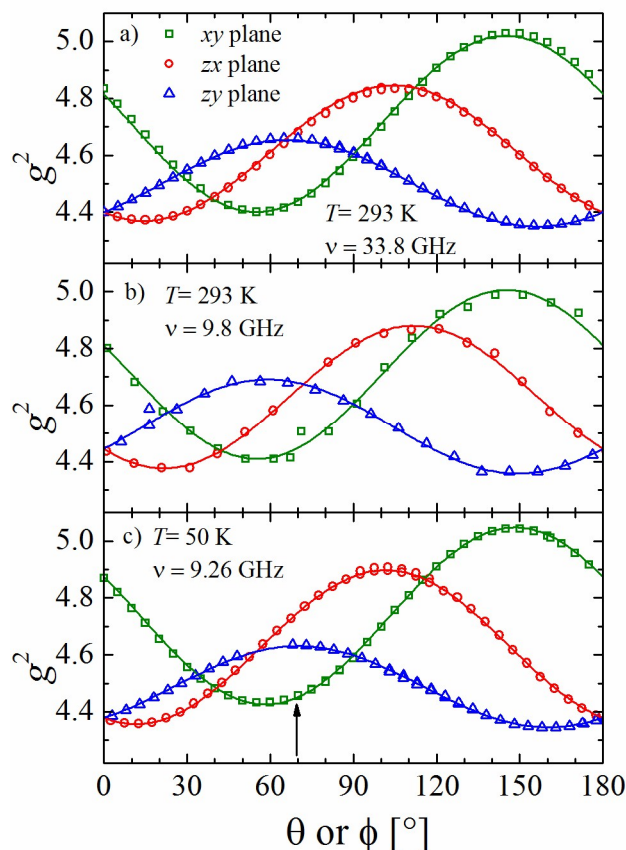


Fig 8 Angular variation of  $g^2(\theta, \phi)$  at a) 33.8 GHz and 293 K, b) 9.8 GHz and 293 K, and c) 9.26 GHz, and 50 K, for  $B_0$  applied in the  $xy$ ,  $zx$  and  $zy$  crystal planes. The solid lines are calculated with the components of the  $g^2$ -matrices given in Table 6. The arrow line in c) indicates the field orientation where the data in Figures 9 were obtained

components, and their variation with the orientation of  $B_0$  allows evaluating the  $\mathbf{A}$  matrices.<sup>25</sup> The binuclear character of a spin system also produces a peculiar hyperfine structure when each electronic spin interacts with its own (Cu) nucleus.<sup>24,25,45</sup> The number of components depends of the total nuclear spin  $^{15}\text{Cu}^1I + \text{Cu}^2I$ , whose values may be 3, 2, 1 or 0, resulting in the seven observed peaks with relative intensities 1:2:3:4:3:2:1 and half the hyperfine parameter  $A$  of the copper ion.<sup>24,45,49</sup> EPR spectra of a binuclear material have four main characteristics: (i) a  $T$  dependence of the intensity of the signals following the so called Bleaney and Bowers equation,<sup>24,25,45</sup> arising from the splitting  $|J_0|$  between singlet and triplet states; (ii) a pattern of the hyperfine structure such as the one described above for the case of two coupled Cu spins, (iii) a “fine structure” arising from the anisotropic spin–spin interaction,  $\mathbf{D}$  term in eqn 2, that splits the electronic signal into two peaks (for  $S = 1/2$  spins), and (iv) a forbidden transition  $\pm 1 \leftrightarrow \mp 1$  within the triplet state at half field of the main transitions, arising from admixtures produced by the  $\mathbf{D}$ -term. Our EPR results above  $\sim 10$  K clearly

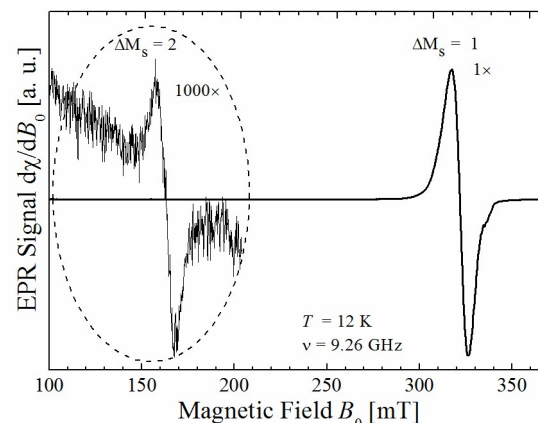


Fig 9 EPR spectrum of **1** observed with  $B_0$  oriented in the  $xy$  plane at  $70^\circ$  of the  $x$  axis. The inset displays with a vertical amplification of 1000 the signal observed around 160 mT.

### 35 The Mononuclear Species

The EPR signals below  $T = 10$  K display hyperfine couplings and are assigned to traces of two types of crystal defects  $M_j$  ( $j = 1, 2$ ) containing mononuclear copper, whose intensities grow as  $1/T$  with decreasing  $T$ . The spin Hamiltonian of each of these defects should consider one copper spin  $\mathbf{S}_{M_j}$  and the corresponding nuclear spins, thus,

$$\mathcal{H}_m(j) = \mu_B \mathbf{B}_0 \cdot \mathbf{g}_{M_j} \cdot \mathbf{S}_{M_j} + I_{Cu_j} \cdot \mathbf{A}_{M_j} \cdot \mathbf{S}_{M_j} + I_{N1_j} \cdot \mathbf{A}_{N1_j} \cdot \mathbf{S}_{M_j} + I_{N2_j} \cdot \mathbf{A}_{N2_j} \cdot \mathbf{S}_{M_j}, j = 1, 2 \quad (3)$$

The results in Figs. 6 and 7a,b allow calculating the matrices  $\mathbf{g}_{M_1}$  and  $\mathbf{A}_{M_1}$  of the mononuclear species  $M_1$ , and the eigenvalues and eigenvectors given in Table 5. The solid lines calculated with these values, are in good agreement with the experimental values for  $M_1$ . The information in Figs. S4<sup>†</sup> and S5a,b<sup>†</sup> for  $M_2$  allow estimating the eigenvalues and eigenvectors of  $\mathbf{g}_{M_2}$  and  $\mathbf{A}_{M_2}$  (Table S1<sup>†</sup>), although with an uncertainty greater than for site  $M_1$ . The eigenvalues of the matrices  $\mathbf{g}_{M_1}$ ,  $\mathbf{g}_{M_2}$ ,  $\mathbf{A}_{M_1}$  and  $\mathbf{A}_{M_2}$  are typical for  $\text{Cu}^{\text{II}}$  in tetragonal configurations of ligands. In addition, the axial eigenvectors  $g_3$  and  $A_3$  of  $M_1$  are nearly equal, as expected.<sup>25,45</sup>

55 Table 5 Eigenvalues and eigenvectors of the  $\mathbf{g}_{M_1}$  and  $\mathbf{A}_{M_1}$  matrices of mononuclear site  $M_1$ , calculated from the EPR results at 4.7 K in Figure 7.

	Eigenvalues	Eigenvectors		
$g_1$	2.068(1)	-0.3(5)	-0.8(5)	0.5(5)
$g_2$	2.069(5)	0.8(5)	0.0(5)	0.6(5)
$g_3$	2.298(1)	-0.557(3)	0.556(2)	0.618(1)
$A_1$	1(1) $10^{-4} \text{ cm}^{-1}$	-0.50(5)	0.39(5)	-0.76(1)
$A_2$	25(1) $10^{-4} \text{ cm}^{-1}$	0.66(3)	0.73(3)	-0.06(5)
$A_3$	181(1) $10^{-4} \text{ cm}^{-1}$	-0.542(1)	0.546(1)	0.638(1)

They form an angle of  $\sim 4^\circ$  with the molecular axial directions (normal to the tetragonal plane) of Cu1 in the structure. The angle between the axial eigenvector of  $\mathbf{g}_{M_2}$  and  $\mathbf{A}_{M_2}$  with the normal to the best plane through the N1B, N2B, O7 and O1 around Cu2 is  $24^\circ$ . The result for site  $M_1$  suggests that it corresponds to units where Cu2 is lacking, and where the molecular distortion of the Cu1 environment is low. We extrapolate and propose that the less abundant mononuclear site  $M_2$  corresponds to binuclear units in which Cu1 is lacking, even though this angle (determined with a much smaller accuracy) is large. The results of these comparisons are displayed in Figs. 10a,b where we show the binuclear molecule, distinguishing sites  $M_1$ , (a), and  $M_2$ , (b), and indicating the direction of the axial eigenvectors of the  $\mathbf{g}$ -matrices in each case. A higher distortion of site  $M_2$  is compatible with the strong constraint imposed by the pyrophosphate bond. Expectedly, charge compensation processes should occur in these sites but they involve non paramagnetic atoms, invisible for EPR. The  $\mathbf{g}$  and  $\mathbf{A}$  matrices of the defects  $M_1$  and  $M_2$  are characteristic of  $\text{Cu}^{\text{II}}$  ions with ground  $d(x^2-y^2)$  orbitals.<sup>25,45,50</sup> As explained before, isotopically enriched single crystals of **1** are expensive to prepare but, since the bulk dinuclear material is not magnetic at low  $T$ , ENDOR experiments in powder samples (using field selection properties<sup>51-53</sup>) may be more convenient to obtain a better structural description. Traces of crystal defects or impurities behaving as paramagnetic  $S = 1/2$  mononuclear entities in binuclear copper compounds are well known in magnetic and EPR measurements,<sup>26,27,30,54,55</sup> but, to our knowledge, this is the first study describing their structures. Their susceptibility and the intensity of the EPR spectra follow a  $1/T$  Curie-Weiss temperature dependence, and the contribution of these traces are relevant at low  $T$  when they are magnetically isolated from the AFM bulk material which is frozen in the singlet state. Zvyagin *et al.*<sup>30</sup> studied by EPR single crystals of the binuclear AFM cyclosilicate  $\text{BaCuSi}_2\text{O}_6$  observing a fine structure ( $\mathbf{D}$ -term) and, below 7 K, the typical hyperfine pattern of mononuclear  $\text{Cu}^{\text{II}}$ .

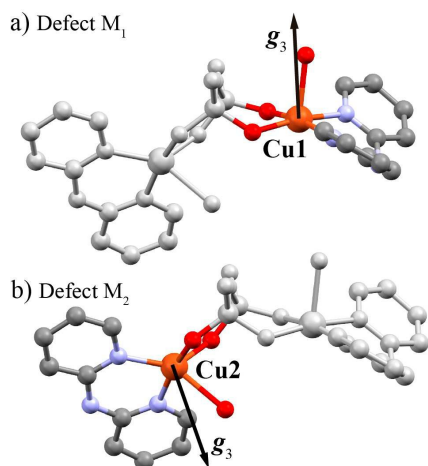


**Fig 10** Comparison of the axial directions of the  $\mathbf{g}$  matrices of mononuclear defect sites  $M_1$  (a) and  $M_2$  (b) with the structural information for Cu1 and Cu2.

## The Exchange

The singlet-triplet splitting  $|J_0|$  introduced by the exchange interaction produces a  $T$  dependence of the intensity of the signal, which for AFM units disappears when  $k_B T \ll |J_0|$  and the triplet state is unpopulated.<sup>24,25,45</sup> This variation was analysed plotting in Fig. 11  $T$  times the ratio  $R(T)$  between the integrated areas of the signals attributed to the sample and that of the paramagnetic  $\text{Cr}^{\text{III}}:\text{MgO}$  marker in the range  $4.7 \text{ K} < T < 50 \text{ K}$ , considering the spectra in Figs. 4 and S1<sup>†</sup>. The corresponding Bleaney-Bowers equation<sup>24,27,31,54</sup> for the susceptibility of binuclear units normalized to 1 for  $T \rightarrow \infty$ , is:

$$T \times R(T) \propto \frac{4}{3 + \exp(-J_0/k_B T)} \quad (4)$$

Fitting eq 4 to the results in Fig. 11 we obtain  $J_0 = -28(3) \text{ cm}^{-1}$ . This procedure avoids difficult absolute measurements of resonance intensities needed to consider changes with  $T$  of the experimental setup.

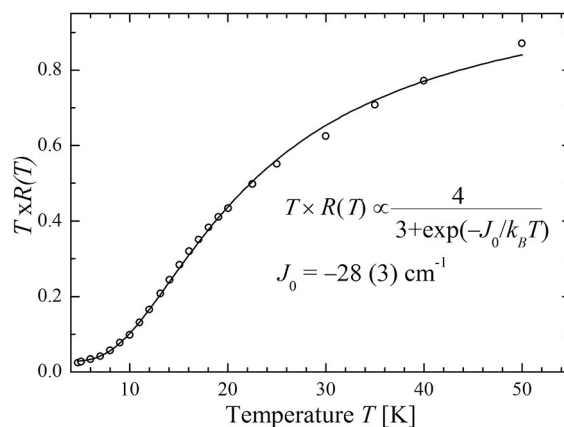


**Fig 11** Temperature variation of  $T$  times the ratio  $R(T)$  between the integrated areas of the signals corresponding to the copper dinuclear unit and the  $\text{Cr}^{\text{III}}$  marker given in Fig 4 (symbols). The solid line is the best fit of the equation of Bleaney and Bowers (eqn 4) to the data.

## Results at High Temperatures

The EPR spectra at 50 K (Fig. 4) and the angular variation of the  $g$ -factor shown in Figs. 8a,b,c at 50 and 293 K are described by an effective spin  $S = 1/2$  with no  $\mathbf{D}$ -term or hyperfine couplings:

$$\mathcal{H}_1 = \mu_B \mathbf{S} \cdot \mathbf{g} \cdot \mathbf{B}_0 \quad (5)$$

resulting from the merging of the fine and hyperfine structures.<sup>56</sup> The observed positions of the single resonance in the three studied planes allow to obtain<sup>48</sup>  $g^2(\theta, \varphi)$  (Figs. 8a,b,c), and calculate the components and the eigenvalues of the  $\mathbf{g}^2$ -matrices given in Table 6. The solid lines in Figs. 8a,b,c mark the values obtained with these matrices. According to the crystallographic results, the matrices  $\mathbf{g}_{\text{Cu1}}$  and  $\mathbf{g}_{\text{Cu2}}$  of the  $\text{Cu}^{\text{II}}$  ions in the binuclear unit defined in eqn 2 should be differently oriented. However, the single line observed for  $T \geq 50 \text{ K}$  indicates that the resonances of the two coppers collapse due to the intrabinuclear exchange interaction, and  $\mathbf{g}_{\text{Cu1}}$  and  $\mathbf{g}_{\text{Cu2}}$  are replaced by their average  $\mathbf{g} = (\mathbf{g}_{\text{Cu1}} + \mathbf{g}_{\text{Cu2}})/2$  of eq 5.<sup>49,56-59</sup> No

information about the individual  $\mathbf{g}$  matrices in the binuclear unit can be obtained.

### Couplings Between Binuclear Units

Changes with  $T$  of the spectra may be produced by exchange interactions between spins in neighbour units  $u$  and  $u'$ :

$$\mathcal{H} = \mathcal{H}_u + \mathcal{H}_{u,u'} \quad (6)$$

where  $\mathcal{H}_u$  is given by eqn 2 and the  $\mathcal{H}_{u,u'}$  are coupling terms. Each binuclear unit sees a different environment, and  $\mathcal{H}_{u,u'}$  has a time dependent distribution of values, consequence of the spin dynamics. Anderson and Weiss<sup>57</sup> and others<sup>58,60,61</sup> showed that a distribution of time dependent exchange couplings may average out the structure of magnetic resonance lines due to dipolar, fine and hyperfine couplings, and these ideas have been used to estimate the magnitude of small exchange interactions from EPR data.<sup>26,27,31,56</sup> The case of interacting binuclear units is particularly attractive because for  $T \ll |J_0/k_B|$ , when the triplet state is unpopulated and the units are frozen in the

**Table 6** Components and eigenvalues of the  $\mathbf{g}^2$  matrices at 50 and 293 K calculated from the EPR data in Figs 8a,b,c and the corresponding eigenvalues at different microwave frequencies ( $\nu$ ) and temperatures ( $T$ ).

$\nu$	33.4 GHz	9.8 GHz	9.4 GHz
$T$	293K	293K	50 K
$(g^2)_{xx}$	4.816(1)	4.811(3)	4.875(1)
$(g^2)_{yy}$	4.604(1)	4.603(3)	4.598(1)
$(g^2)_{zz}$	4.399(1)	4.445(3)	4.378(1)
$(g^2)_{xz}$	-0.291(1)	-0.279(4)	-0.278(1)
$(g^2)_{zx}$	-0.116(1)	-0.173(4)	-0.107(1)
$(g^2)_{zy}$	0.112(1)	0.146(4)	0.090(1)
$(g^2)_1$	4.349(1)	4.357(2)	4.345(1)
$(g^2)_2$	4.412(1)	4.416(3)	4.430(1)
$(g^2)_3$	5.059(1)	5.085(2)	5.075(1)

ground singlet these are non-magnetic. As displayed in Fig. 12 the population of the triplet state increases as the temperature increases, triggering the interaction  $\mathcal{H}_{u,u'}$  and making the singlet-triplet excitations mobile, as described by the so-called triplet excitations or triplons analysed by their effect in magnetic resonance,<sup>22,27,49</sup> and other perspectives.<sup>21,23</sup> The population of the triplet state in compound **1** allows observing the typical binuclear hyperfine structure at  $\sim 10$  K (Figs. 4d and S3); at larger  $T$  (Fig. 4e), the number of triplet excitations increases, broadening the spatial dispersion of the triplet state, and averaging out this structure. In compound **1** anisotropic exchange and dipole-dipole interactions ( $\mathbf{D}$  term in eqn 2) may be estimated obtaining a value  $|D| \sim 0.022 \text{ cm}^{-1}$ . The observed lack of fine structure at any  $T$  is attributed to interbinuclear exchange coupling terms,<sup>26,27</sup> that average out the spin-spin terms and allow estimating a lower limit  $|J_1| > 0.022 \text{ cm}^{-1}$  for the rms exchange interaction between coppers in neighbour units.<sup>62</sup>

### The Half Field Resonance

Even when the structure of the spectrum expected for the binuclear unit of **1** does not show a splitting due to the anisotropic spin-spin interaction  $D$ , it displays a half field resonance attributed to the same interaction.<sup>25</sup> We have a simple explanation to this previously unexplored problem: the splitting of the depends linearly with the  $D$  parameter<sup>25</sup> while the intensity of the half field transition is proportional to  $D^2$ .<sup>28,29</sup> Thus, the modulation of the spin-spin interaction introduced by the exchange coupling between units averages to zero the splitting but does not destroy the forbidden transition. In an important contribution Eaton *et al.*<sup>28</sup> showed in 1983 that the forbidden resonance observed at half field allows to calculate the magnitude of the anisotropic spin-spin coupling  $D$  and the distance between spins in the dinuclear unit. Considering the ratio  $R = 1/1000$  between the areas of the forbidden and the allowed peaks, we estimate<sup>28,29</sup>  $D \sim 0.022 \text{ cm}^{-1}$ , in close agreement with the value estimated using the point dipolar approximation. This result sets a lower limit  $|J_1| \geq D$  to the interaction between copper ions in neighbor dinuclear units, that averages out the structure introduced by the  $D$  term.

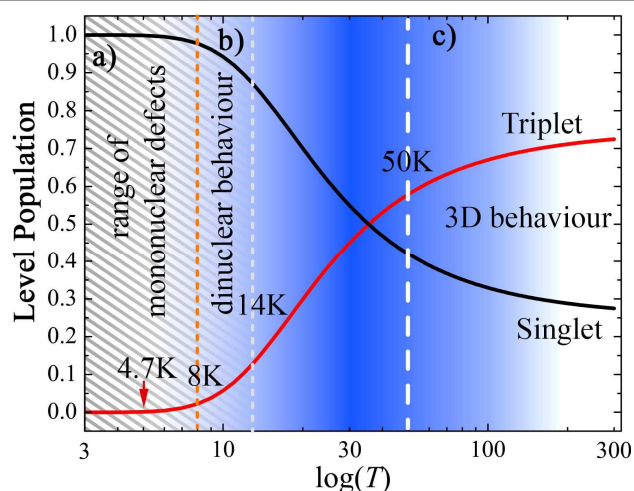


**Fig 12** Populations of the singlet and triplet level of the binuclear unit as a function of temperature. The figure emphasizes the behaviour of the EPR spectrum arising from these populations. Temperature regions a), b) and c) are described in the text.

### Discussion and Conclusions

The EPR signals of binuclear  $[\text{Cu}_2(\text{bpa})_2(\text{P}_2\text{O}_7)(\text{H}_2\text{O})_2] \cdot 2.5\text{H}_2\text{O}$ , **1**, observed between  $\sim 4.7$  and 8 K (range (a) in Fig. 12), are attributed to traces of two species of mononuclear defects  $M_1$  and  $M_2$  with  $S = 1/2$ , each having one  $\text{Cu}^{\text{II}}$  ion, with signal intensities increasing with decreasing  $T$ , and two N ligands, as for Cu1 and Cu2 in the structure of **1**. Comparing the principal directions of the  $\mathbf{g}$  and  $\mathbf{A}$  matrices with the molecular directions of Cu1 and Cu2 (Figs. 10a,b) the agreement is good for site  $M_1$ , and only acceptable for site  $M_2$  if one considers the uncertainties of their  $\mathbf{g}$  and  $\mathbf{A}$  matrices and a large site distortion for  $M_2$ . Crystal defects may originate during the crystallization of **1** from a solution expected to have a variety of other  $\text{Cu}^{\text{II}}$  pyrophosphate species containing bpa. Our measurements show

that the quantity and properties of the defects do not change qualitatively or quantitatively with the cycling of  $T$ . No structural transitions are shown by the EPR results.

The complex  $T$  dependence of the spectra above 8 K is consequence of the interplay between the AFM binuclear exchange interaction  $J_0$  and a much smaller exchange interaction  $J_1$  coupling neighbouring units, offering information about the magnetic behaviour of **1**. In range (b) of Fig. 12 between 8 K and 18 K, when the population of the triplet state is small but rapidly increasing, and triplet excitations travel freely in the material, one observes a binuclear behaviour characterized by the hyperfine structure and the  $T$  variation of the signal intensity, attributed to weakly interacting binuclear units. Hyperfine coupling with the two copper nuclei in the units shows up above  $\sim 8$  K and collapses at  $\sim 14$  K. Above 18 K (range (c)) the hyperfine structure is destroyed by the increase of magnetic excitations and the delocalization of the triplet states, indicating that the excitations produce a spin dynamics faster than the characteristic times related to the hyperfine coupling. The intensity of the signal (a static equilibrium property) follows the Bleaney and Bowers equation for the binuclear susceptibility, consequence of the singlet–triplet splitting  $|J_0|$ . The high  $T$  behaviour is attributed to a 3D array of coupled interacting binuclear units and the single line observed in the range (c) of Fig. 12 results from averaging out the differences in the  $g$ -factors of Cu1 and Cu2, and merging the hyperfine structures with the nuclei of Cu and N, and the fine structure term  $D$ .

The exchange coupling  $J_0 = -28(3) \text{ cm}^{-1}$  calculated from the  $T$  variation of the signal intensity of **1** is one order of magnitude larger than those estimated for the four binuclear copper compounds bridged by protonated pyrophosphates,<sup>19</sup> indicating a more effective exchange path between Cu1 and Cu2 (Cu1–O2–P1–O1–Cu2 and Cu1–O6–P2–O7–Cu2) for the structure described in Fig. 2. A similar value,  $J_0 = -20 \text{ cm}^{-1}$ , was obtained from susceptibility measurements for the compound [Cu(bipy)H<sub>2</sub>O]<sub>2</sub>P<sub>2</sub>O<sub>7</sub>·7H<sub>2</sub>O studied by Kruger *et al.*,<sup>5</sup> with a very similar Cu<sup>II</sup> pyrophosphate-bridged core. Experiments and DFT calculations, have shown however, that several other factors such as exact bridging angles, orbitals involved, pyrophosphate protonation and hydration, play a role in mediating magnetic interactions between Cu<sup>II</sup> ions.<sup>18,63,64</sup> Our results add more evidence of the relevant effects of all such factors.

#### Acknowledgments

We are grateful to the referees for suggestions that contributed to make further progresses in our work. MP and RC are members of CONICET. We acknowledge support from CAI+D, Universidad Nacional del Litoral in Argentina, and from PRONEX/FAPESP, FAPERJ and CNPq in Brazil.

#### Notes and references

a Facultad de Bioquímica y Ciencias Biológicas, Universidad Nacional del Litoral, Ciudad Universitaria, 3000 Santa Fe,

Argentina. E-mail sartoris@fbc.unl.edu.ar

b Grupo de Biofísica Molecular Sergio Mascarenhas, Departamento de Física e Ciência Interdisciplinar, Instituto de Física de São Carlos, Universidade de São Paulo, CP 369, 13560-970 São Carlos,, SP, Brazil.

c Instituto de Física, Universidade Federal de Goiás, Campus Samambaia, CP 131, 74001-970, Goiânia, GO, Brazil.

d Facultad de Ciencias Exactas y Naturales, INQUIMAE-DQIAQF, Universidad de Buenos Aires, Ciudad Universitaria, 1428 Buenos Aires, Argentina.

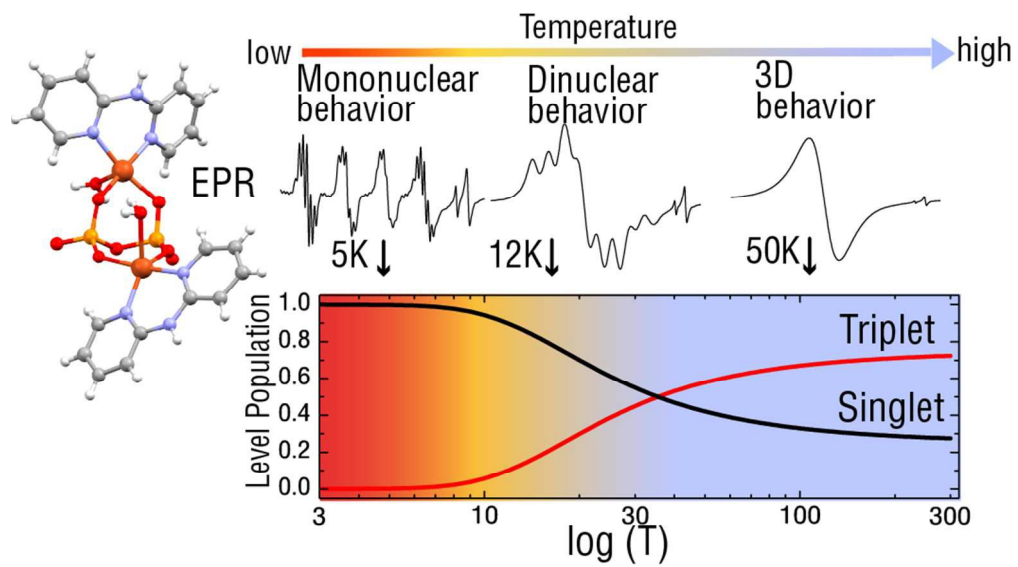
e Comisión Nacional de Energía Atómica, Av. General Paz 1499, 1650 San Martín, Buenos Aires, Argentina.

f Instituto de Física del Litoral (CONICET-UNL), Güemes 3450, 3000 Santa Fe, Argentina. E-mail: calvo.rafael@conicet.gov.ar

† Electronic supplementary information (ESI) available: Relevant magnetic data and crystallographic information files are given in ESI. CCDC 1004333 contains the supplementary crystallographic data for this paper. These data can be obtained free of charge from The Cambridge Crystallographic Data Centre via [www.ccdc.cam.ac.uk/data\\_request](http://www.ccdc.cam.ac.uk/data_request). See DOI: 10.1039/b000000x/. ESI also contains Fig. S1 and S2 complementing Fig. 4; Fig. S3 showing the binuclear hyperfine structure at 12 K; Fig. S4 displaying the angular variations of  $g$  and  $A$  for mononuclear site M<sub>2</sub>. Fig. S5 displays the values of  $g^2$  and  $g^2A^2$  for site M<sub>2</sub>, calculated from the data Table S1 contains eigenvalues and eigenvectors of matrices  $g$  and  $A$  for mononuclear site M<sub>2</sub>. Fig. 6 display the second integral of the main peak and the half field peak. Fig. S7 show spectra of the half field peak as a function of  $T$ .

- O. F. Ikotun, N. Marino, P. E. Kruger, M. Julve, and R. P. Doyle, *Coord. Chem. Rev.*, 2010, **254**, 890–915.
- R. R. Crichton, *Biological Inorganic Chemistry. A New Introduction to Molecular Structure and Function*, Elsevier, Amsterdam, 2nd Ed., 2012.
- R. N. Bose, R. J. Maurmann, R. J. Mishur, L. Yasui, S. Gupta, W. S. Grayburn, H. Hofstetter, and T. Salley, *Proc. Natl. Acad. Sci. USA*, 2008, **105**, 18314–18319.
- O. F. Ikotun, E. M. Higbee, W. Ouellette, and R. P. Doyle, *J. Inorg. Biochem.*, 2009, **103**, 1254–1264.
- P. E. Kruger, R. P. Doyle, M. Julve, F. Lloret, and M. Nieuwenhuyzen, *Inorg. Chem.*, 2001, **40**, 1726–1727.
- N. Marino, A. R. Vortherms, A. E. Hoffman, and R. P. Doyle, *Inorg. Chem.*, 2010, **49**, 6790–6792.
- R. P. Doyle, P. E. Kruger, B. Moubaraki, S. Murray, M. Nieuwenhuyzen, and K. S. Murray, *Dalt. Trans.*, 2003, 4230–4237.
- R. P. Doyle, M. Nieuwenhuyzen, and P. E. Kruger, *Dalt. Trans.*, 2005, 3745–3750.
- R. P. Doyle, T. Bauer, M. Julve, F. Lloret, J. Cano, M. Nieuwenhuyzen, and P. E. Kruger, *Dalt. Trans.*, 2007, 5140–5147.
- O. F. Ikotun, N. G. Armatus, M. Julve, P. E. Kruger, F. Lloret, M. Nieuwenhuyzen, and R. P. Doyle, *Inorg. Chem.*, 2007, **46**, 6668–6674.
- O. F. Ikotun, E. M. Higbee, W. Ouellette, F. Lloret, M. Julve, and R. P. Doyle, *Eur. J. Inorg. Chem.*, 2008, 5281–5286.
- N. Marino, C. H. Fazén, J. D. Blakemore, C. D. Incarvito, N. Hazari, and R. P. Doyle, *Inorg. Chem.*, 2011, **50**, 2507–2520.
- N. Marino, S. K. Hanson, P. Müller, and R. P. Doyle, *Inorg. Chem.*, 2012, **51**, 10077–10079.
- P. Heikinheimo, P. Pohjanjoki, A. Helminen, M. Tasanen, B. S. Cooperman, A. Goldman, A. Baykov, and R. Lahti, *Eur. J. Biochem.*, 1996, **239**, 138–143.
- P. Heikinheimo, V. Tuominen, A. K. Ahonen, A. Teplyakov, B. S. Cooperman, A. A. Baykov, R. Lahti, and A. Goldman, *Proc. Natl. Acad. Sci. U. S. A.*, 2001, **98**, 3121–3126.

16. E. W. Ainscough, M. Brodie, J. D. Ranford, J. M. Waters, and K. S. Murray, *Inorg. Chim. Acta*, 1992, **197**, 107–115.
17. J.-Y. Xu, J.-L. Tian, Q.-W. Zhang, J. Zhao, S.-P. Yan, and D.-Z. Liao, *Inorg. Chem. Commun.*, 2008, **11**, 69–72.
18. N. Marino, O. F. Iktoun, M. Julve, F. Lloret, J. Cano, and R. P. Doyle, *Inorg. Chem.*, 2011, **50**, 378–389.
19. R. P. Sartoris, R. Calvo, R. C. Santana, O. R. Nascimento, M. Perec, and R. F. Baggio, *Polyhedron*, 2014, **79**, 178–185.
20. M. Perec, R. P. Sartoris, R. Calvo, and R. Baggio, *Inorg. Chem. Commun.*, 2012, **22**, 141–145.
21. V. Zapf, M. Jaime, and C. D. Batista, *Rev. Mod. Phys.*, 2014, **86**, 563–614.
22. P. L. Nordio, Z. G. Soos, and H. M. McConnell, *Annu. Rev. Phys. Chem.*, 1966, **17**, 237–260.
23. S. Sachdev and R. N. Bhatt, *Phys. Rev. B*, 1990, **41**, 9323–9328.
24. B. Bleaney and K. D. Bowers, *Proc. R. Soc. A, London*, 1952, **214**, 451–465.
25. J. A. Weil and J. R. Bolton, *Electron Paramagnetic Resonance. Elementary Theory and Practical Applications*, Wiley-Interscience, Hoboken, New Jersey, 2nd edn., 2007.
26. M. Perec, R. Baggio, R. P. Sartoris, R. C. Santana, O. Peña, and R. Calvo, *Inorg. Chem.*, 2010, **49**, 695–703.
27. R. Calvo, J. E. Abud, R. P. Sartoris, and R. C. Santana, *Phys. Rev. B*, 2011, **84**, 104433.
28. S. S. Eaton, K. M. More, B. M. Sawant, and G. R. Eaton, *J. Am. Chem. Soc.*, 1983, **105**, 6560–6567.
29. R. E. Coffman and A. Pezeshk, *J. Magn. Reson.*, 1986, **70**, 21–33.
30. S. A. Zvyagin, J. Wosnitza, J. Krzystek, R. Stern, M. Jaime, Y. Sasago, and K. Uchinokura, *Phys. Rev. B*, 2006, **73**, 094446.
31. L. M. B. Napolitano, O. Nascimento, S. Cabaleiro, J. Castro, and R. Calvo, *Phys. Rev. B*, 2008, **77**, 214423.
32. CrysAlisPRO, *Oxford Diffraction Ltd.*, Oxfordshire, England, 2007.
33. G. M. Sheldrick, *Acta Crystallogr. A, Found. Crystallogr.*, 2008, **64**, 112–122.
34. A. L. Spek, *Acta Crystallogr. D*, 2009, **65**, 148–155.
35. F. H. Allen, *Acta Crystallogr. B*, 2002, **58**, 380–388.
36. C. F. Macrae, P. R. Edgington, P. McCabe, E. Pidcock, G. P. Shields, R. Taylor, M. Towler, and J. van de Streek, *J. Appl. Crystallogr.*, 2006, **39**, 453–457.
37. C. F. Macrae, I. J. Bruno, J. A. Chisholm, P. R. Edgington, P. McCabe, E. Pidcock, L. Rodriguez-Monge, R. Taylor, J. van de Streek, and P. A. Wood, *J. Appl. Crystallogr.*, 2008, **41**, 466–470.
38. C. Giacovazzo, *Fundamentals of Crystallography*, Oxford Science Publications, Oxford, 3rd edn., 2011.
39. S. Stoll and A. Schweiger, *J. Magn. Reson.*, 2006, **178**, 42–55.
40. Matlab, *The Mathworks Inc.*, The Mathworks Inc., Natick, MA 01760, 2012.
41. I. D. Brown, *The Chemical Bond in Inorganic Chemistry: The Bond-Valence Model*, 2002.
42. A. W. Addison, T. N. Rao, J. Reedijk, J. van Rijn, and G. C. Verschoor, *J. Chem. Soc. Dalton Trans.*, 1984, 1349–1356.
43. R. Calvo, M. C. G. Passeggi, R. A. Isaacson, M. Y. Okamura, and G. Feher, *Biophys. J.*, 1990, **58**, 149–165.
44. E. Garribba, G. Micera, D. Sanna, and L. Strinna-Erre, *Inorg. Chim. Acta*, 2000, **299**, 253–261.
45. A. Abragam and B. Bleaney, *Electron Paramagnetic Resonance of Transition Ions*, Clarendon Press, Oxford, 1970.
46. J. R. Wasson, C.-I. Shyr, and C. Trapp, *Inorg. Chem.*, 1968, **7**, 469–473.
47. J. A. Weil, *J. Magn. Reson.*, 1975, **18**, 113–116.
48. R. Calvo, S. B. Oseroff, and H. C. Abache, *J. Chem. Phys.*, 1980, **72**, 760–767.
49. A. Bencini and D. Gatteschi, *Electron Paramagnetic Resonance of Exchange Coupled Systems*, Springer-Verlag, Berlin, 1st edn., 1990.
50. E. Garribba and G. Micera, *J. Chem. Educ.*, 2006, **83**, 1229–1232.
51. M. Flores, R. A. Isaacson, R. Calvo, G. Feher, and W. Lubitz, *Chem. Phys.*, 2003, **294**, 401–413.
52. M. Flores, R. Isaacson, E. C. Abresch, R. Calvo, W. Lubitz, and G. Feher, *Biophys. J.*, 2006, **90**, 3356–3362.
53. M. Flores, R. Isaacson, E. C. Abresch, R. Calvo, W. Lubitz, and G. Feher, *Biophys. J.*, 2007, **92**, 671–682.
54. O. Kahn, *Molecular Magnetism*, Wiley VCH, New York, 1993.
55. V. Paredes-García, R. C. Santana, R. Madrid, A. Vega, E. Spodine, and D. Venegas-Yazigi, *Inorg. Chem.*, 2013, **52**, 8369–8377.
56. R. Calvo, *Appl. Magn. Reson.*, 2007, **31**, 271–299.
57. P. W. Anderson and P. R. Weiss, *Rev. Mod. Phys.*, 1953, **25**, 269–276.
58. P. W. Anderson, *J. Phys. Soc. Jpn.*, 1954, **9**, 316–339.
59. R. Calvo, M. A. Mesa, G. Oliva, J. Zukerman-Schpector, O. R. Nascimento, M. Tovar, and R. Arce, *J. Chem. Phys.*, 1984, **81**, 4584–4591.
60. R. Kubo and K. Tomita, *J. Phys. Soc. Jpn.*, 1954, **9**, 888–919.
61. G. E. Pake, *Paramagnetic Resonance. An Introductory Monograph*, Benjamin, Inc., New York, First Ed., 1962.
62. M. C. G. Passeggi and R. Calvo, *J. Magn. Reson.*, 1989, **81**, 378–382.
63. S. Salunke, V. R. Singh, A. V. Mahajan, and I. Dasgupta, *J. Phys. Condens. Matter*, 2009, **21**, 025603.
64. O. Janson, A. A. Tsirlin, J. Sichelschmidt, Y. Skourski, F. Weickert, and H. Rosner, *Phys. Rev. B*, 2011, **83**, 094435.



89x49mm (300 x 300 DPI)